



Delft University of Technology

Creation of complex nano-interferometric field structures

Man, Zhongsheng; Meng, Peiwen; Fu, Shenggui

DOI

[10.1364/OL.45.000037](https://doi.org/10.1364/OL.45.000037)

Publication date

2019

Document Version

Final published version

Published in

Optics Letters

Citation (APA)

Man, Z., Meng, P., & Fu, S. (2019). Creation of complex nano-interferometric field structures. *Optics Letters*, 45(1), 37-40. <https://doi.org/10.1364/OL.45.000037>

Important note

To cite this publication, please use the final published version (if applicable).
Please check the document version above.

Copyright

Other than for strictly personal use, it is not permitted to download, forward or distribute the text or part of it, without the consent of the author(s) and/or copyright holder(s), unless the work is under an open content license such as Creative Commons.

Takedown policy

Please contact us and provide details if you believe this document breaches copyrights.
We will remove access to the work immediately and investigate your claim.

Creation of complex nano-interferometric field structures

ZHONGSHENG MAN,^{1,2,3,4} PEIWEI MENG,² AND SHENGGUI FU^{1,5}

¹School of Physics and Optoelectronic Engineering, Shandong University of Technology, Zibo 255000, China

²Optics Research Group, Delft University of Technology, Department of Imaging Physics, Lorentzweg 1, 2628CJ Delft, The Netherlands

³Collaborative Innovation Center of Light Manipulations and Application, Shandong Normal University, Jinan 250358, China

⁴e-mail: zsman@sdut.edu.cn

⁵e-mail: fushenggui@sdut.edu.cn

Received 5 August 2019; revised 22 October 2019; accepted 7 November 2019; posted 8 November 2019 (Doc. ID 374530); published 16 December 2019

With dual two-dimensional Airy-like waveforms, we demonstrate the creation of highly confined electromagnetic fields in the transverse plane and circular or elliptical propagation trajectories in the longitudinal plane by using specially designed Pancharatnam–Berry (PB) phases. Applying the Richards and Wolf vectorial diffraction methods, the explicit expressions are obtained to calculate the strength vectors and energy flux of the three-dimensional electromagnetic fields. Calculations reveal that the nano-interferometric structures of such highly confined fields highly depend on the indexes γ_1 and γ_2 determining the PB phase, thereby enabling the engineering of highly confined fields with tunable size, spacing, and propagation trajectories. © 2019 Optical Society of America

<https://doi.org/10.1364/OL.45.000037>

In 1979, the concept of the self-accelerating wave packet was proposed in the pioneering work of Berry and Balazs, who theoretically predicted that the Schrödinger equation with a spatially uniform force term has as a solution for a nonspreading Airy wave packet [1]. However, this work remained relatively unnoticed for decades, possibly because the Airy waveform has infinite norm or because producing particles in an Airy state is difficult. It was not until 2007 that the first observation of Airy beams emerged [2,3]. As opposed to other diffraction-free beams previously studied, the intensity structure of an Airy beam follows a curved parabolic trajectory. This fascinating feature has been used in a wide range of applications, including plasma guidance [4], microscopy [5,6], and optical micromanipulation [7]. In addition, research has devoted much effort in inducing light fields capable of propagating along other flexible trajectories in free space. To mention a few examples, light beams that travel along circular, elliptical, arbitrary convex, and spiral trajectories have been identified [8–10].

Generally, the aforementioned propagation trajectory control of light beams in free space is based on dynamic phase modulations realized by spatial light modulators, liquid crystals, nonlinear processing, or phase masks. In addition, there is currently substantial interest in highly confined structured fields;

specifically, the creation of customized light fields of nanoscale size to suit specific needs in applications [11–13]. So far, however, attempts to target complex trajectory structures of these highly confined fields have not yet been pursued. Such field distributions can be generated, for instance, by tight focusing of polarized light beams. Under these circumstances, nonparaxial beam configurations are required, and the Pancharatnam–Berry (PB) phase [14–17] rather than the dynamic phase plays the dominant role in forming these field structures.

In this Letter, we show that a highly confined field exhibiting dual two-dimensional (2D) Airy-like patterns in the transverse plane and circular and elliptical propagation trajectories in the longitudinal plane is indeed possible when assisted by a tailored PB phase. To this end, using Richards and Wolf vectorial diffraction methods, the explicit expressions to calculate the strength vector and energy flux of the three-dimensional (3D) electric and magnetic fields are presented. By calculations, the intensity structure of the highly confined field is found to depend highly on the indexes γ_1 and γ_2 in the PB phase. The size of the twin Airy-like fields and spacing between them are both controllable and depend highly on the indexes γ_1 and γ_2 in the PB phase, respectively. Both γ_1 and γ_2 have an effect on the propagation trajectory. To gain a better understanding of the proposed complex nano-interferometric fields, the energy fluxes of such highly confined fields are also studied in detail.

Highly confined optical fields can be obtained, for example, by focusing the light beam with an objective lens of high numerical aperture (NA), as depicted in Fig. 1(a). Generally, light from a laser without a specially designed cavity is linearly polarized and is tightly focused to generate a sharp hot-spot field distribution with an elliptical pattern. The state of polarization (SoP) of an arbitrary linearly polarized beam is mathematically written as

$$\mathbf{v}_1 = \cos h \mathbf{e}_x + \sin h \mathbf{e}_y = \frac{1}{\sqrt{2}} \exp(-ih) \mathbf{e}_l + \frac{1}{\sqrt{2}} \exp(ih) \mathbf{e}_r, \quad (1)$$

where \mathbf{e}_x , \mathbf{e}_y , \mathbf{e}_l , and \mathbf{e}_r denote the unit vectors corresponding to x -directed and y -directed linear polarizations and to left-handed (LH) and right-handed (RH) circular polarizations.

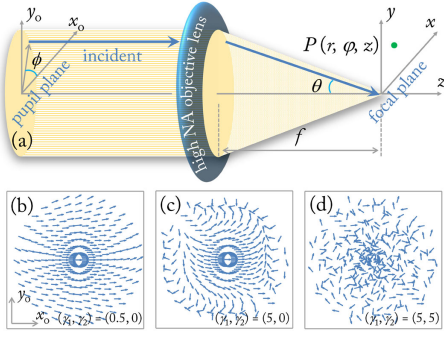


Fig. 1. (a) Schematic diagram for the high NA objective lens focusing system. Here, the geometrical focus is located at the origin of a Cartesian coordinate system, and the propagation axis is z . Polarization distributions for three different input optical fields with $(\gamma_1, \gamma_2) =$ (b) $(0.5, 0)$, (c) $(5, 0)$, and (d) $(5, 5)$ when $h = 0$.

Angle h specifies the orientation of the linearly polarized beam with respect to the x axis. However, if the LH and RH polarization components in Eq. (1) acquire PB phases of σ and $-\sigma$, respectively, the resultant SoP becomes

$$\begin{aligned} \mathbf{v}_2 &= \frac{1}{\sqrt{2}} \exp[-i(h + \sigma)] \mathbf{e}_l + \frac{1}{\sqrt{2}} \exp[i(h + \sigma)] \mathbf{e}_r \\ &= \cos(h + \sigma) \mathbf{e}_x + \sin(h + \sigma) \mathbf{e}_y. \end{aligned} \quad (2)$$

PB phases are related to variations in the SoP, which is much different from the well-known dynamic phases. Significant success has been achieved in producing the above polarization transformations with subwavelength gratings, specially designed wave plates, or optical systems [18–20]. From theory, the PB phase σ in Eq. (2) can have any form of distribution. The creation of highly confined twin Airy-like beams is possible when setting $\sigma = \gamma_1(\rho/\rho_0)^3(\sin^3\phi + \cos^3\phi) + 2\pi\gamma_2\rho/\rho_0(\sin\phi + \cos\phi)$, where γ_1 and γ_2 denote the phase indexes, ρ and ϕ are the polar radius and azimuthal angle in the polar coordinate system, respectively, and ρ_0 is the size of the input field. As examples, Figs. 1(b) and 1(c) show the polarization distributions of three polarized beams with $(\gamma_1, \gamma_2) = (0.5, 0)$, $(5, 0)$, and $(5, 5)$ when $h = 0$, respectively. These distributions are very similar to those of linearly polarized beams for low values of γ_1 [Fig. 1(b)]. However, they change considerably as γ_1 increases [Fig. 1(c)]. Further, for nonzero γ_2 , the polarization becomes more complicated [Fig. 1(d)]. Strongly focused beams have been analyzed by the Richards and Wolf vectorial diffraction theory [21], where they have been proved to fit well with experimental data [22]. The electric and magnetic fields at an observation point $P(r, \phi, z)$ in the focal volume of a high NA objective lens can be obtained as [21]

$$\begin{aligned} \begin{bmatrix} \mathbf{E}(r, \phi, z) \\ \mathbf{H}(r, \phi, z) \end{bmatrix} &= \frac{-ikf}{2\pi} \int_0^{2\pi} \int_0^\alpha \sqrt{\cos\theta} l(\theta) \sin\theta \begin{bmatrix} \mathbf{V}_e \\ \mathbf{V}_h \end{bmatrix} \\ &\cdot \exp\{ik[-r \sin\theta \cos(\phi - \varphi) \\ &+ z \cos\theta]\} d\phi d\theta, \end{aligned} \quad (3)$$

where k and f denote the wave number and focal length, respectively; θ is the tangential angle with respect to the z -axis; $\alpha = \arcsin(\text{NA})/n$, with NA as the numerical aperture of the focusing objective lens and n as the refractive index in the image space that is set to 1 in our configuration; $l(\theta)$ describes the complex amplitude distribution of the incident beam, which we take to be [23]

$$l(\theta) = \exp\left[-\beta^2\left(\frac{\sin\theta}{\sin\alpha}\right)^2\right] J_1\left(2\beta\frac{\sin\theta}{\sin\alpha}\right), \quad (4)$$

where β is the ratio of the pupil radius to the beam waist, and J_1 denotes the first-order Bessel function of the first kind.

In Eq. (3), \mathbf{V}_e represents the electric field polarization vector in the image space contributed by the input SoP; its three mutually perpendicular components V_{ex} , V_{ey} , and V_{ez} are found to be

$$V_{ex} = -\sin\phi \sin T + \cos\theta \cos\phi \cos T, \quad (5)$$

$$V_{ey} = \cos\phi \sin T + \cos\theta \sin\phi \cos T, \quad (6)$$

$$V_{ez} = \sin\theta \cos T, \quad (7)$$

where

$$\begin{aligned} T &= \gamma_1 \left(\frac{\sin\theta}{\sin\alpha}\right)^3 (\cos^3\phi + \sin^3\phi) \\ &+ 2\pi\gamma_2 \left(\frac{\sin\theta}{\sin\alpha}\right) (\cos\phi + \sin\phi) + h - \phi. \end{aligned} \quad (8)$$

We now explore the nano-interferometric behaviors of the electric field based on Eqs. (2)–(8). As examples, Fig. 2 shows the normalized electric field distributions in the focal plane of four different optical fields with $(\gamma_1, \gamma_2) = (0.5, 0)$, $(5, 0)$, $(10, 0)$, and $(15, 0)$ when $h = 0$. Overall, for all four inputs, the transverse components [Figs. 2(a), 2(d), 2(g), and 2(j)] are always much stronger than the longitudinal ones [Figs. 2(b), 2(e), 2(h), and 2(k)] and dominate the total fields. However, in detail, they are very different. Specifically, when the value of γ_1 is low, the hot-spot field distribution exhibits an elliptical pattern for the total field arising from the fact that the polarization distribution is very similar to that of a linearly polarized beam in this situation [Fig. 1(a)]. The full width at half-maximum values of the transverse [Fig. 2(a)] and total [Fig. 2(c)] focal spots are calculated to be about 0.588λ and 0.734λ in the x axis direction and 0.516λ and 0.516λ in the y axis direction, respectively. However, dual Airy-like patterns emerge for the transverse and total field with increasing γ_1 [Figs. 2(d), 2(f), 2(g), 2(i), 2(j), and 2(l)]. Most importantly, controlled by γ_1 , their size is tunable and increases with increasing γ_1 . As a result, targeting a desirable size in highly confined fields to meet different applications can be realized just by carefully tailoring the phase index γ_1 in the PB phase. The spacing between the dual Airy-like fields may be another important indicator for evaluating their quality, which is also controllable in our approach; see Fig. 3. Obviously, with increasing positive γ_2 , the dual highly confined Airy-like fields move radially outward at angles of $\pi/4$ and $5\pi/4$ with respect to the x axis [Figs. 3(a)–3(f)], resulting in a tunable spacing between the fields. Intriguingly, the size of each Airy-like field nearly shows no change, which is very

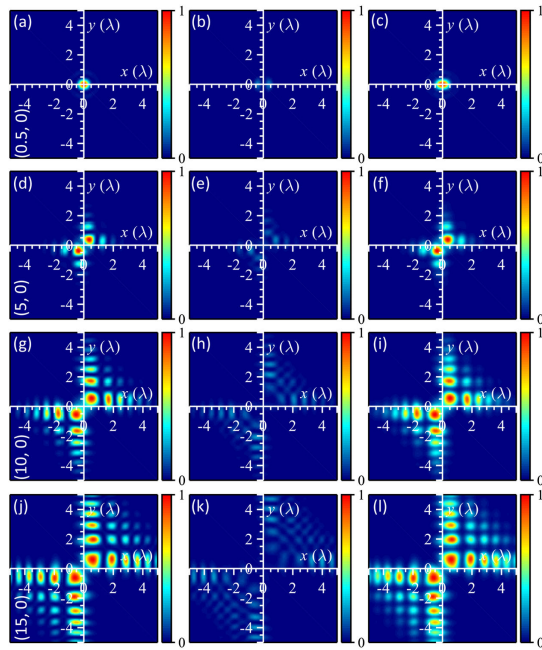


Fig. 2. Calculated electric field intensity distributions in the focal plane of four input optical fields with $(\gamma_1, \gamma_2) = (0.5, 0)$, $(5, 0)$, $(10, 0)$, and $(15, 0)$ in the four rows from top down for $b = 0$ and $(\text{NA}, \beta) = (0.95, 1)$. From left to right, the columns show the transverse and longitudinal field components and the total fields. All intensity distributions are normalized to the maximum intensity in the focal plane for each input light mode. The size for each image is $10\lambda \times 10\lambda$.

important in practical applications. Furthermore, achieving opposite movements in the dual Airy-like fields is also possible if γ_2 is negative [Figs. 3(g)–3(i)]. Here, a quasi-optical lattice is obtained, resulting from the overlap of the dual Airy-like fields.

The propagation dynamics of the highly confined fields in the through-focus plane at angle $\pi/4$ to the $x - z$ plane is depicted in Fig. 4, with $(\gamma_1, \gamma_2) = (10, -2)$, $(10, 2)$, and $(15, 2)$ when $b = 0$. Note that they all exhibit curved propagation trajectories, which are completely different from previously reported results. Specifically, the highly confined fields follow dual circular trajectories [Figs. 4(a) and 4(c)]. Furthermore, they swap positions under a change in the sign of γ_2 , resulting in an incomplete ring pattern along the propagation direction [Figs. 4(d) and 4(f)]. Moreover, the circular trajectories evolve into ellipses when γ_2 increases [Figs. 4(g) and 4(i)]. Hence, highly confined fields capable of propagating along tunable trajectories can be achieved.

By calculations, it is found that the values of NA and β affect the size and propagation distance of the highly confined Airy-like fields greatly, as can be seen in Fig. 5, which shows the normalized total electric field distributions in the focal and through-focus planes with $(\text{NA}, \beta) = (0.7, 1)$, $(0.8, 1)$, and $(0.8, 1.5)$ when $(\gamma_1, \gamma_2) = (10, 2)$ and $b = 0$. Obviously, the size in the focal plane and propagation distance in the through-focus plane of the highly confined Airy-like field both decrease when NA changes from 0.7 to 0.8, which can further decrease with the increase of β .

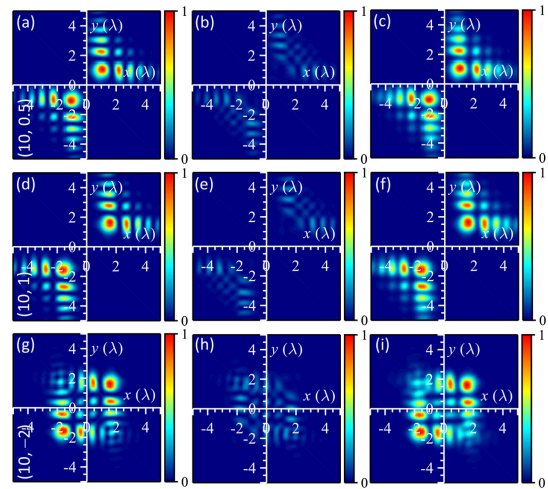


Fig. 3. Calculated electric field intensity distributions in the focal plane of three input optical fields with $(\gamma_1, \gamma_2) = (10, 0.5)$, $(10, 1)$, and $(10, -2)$ in the three rows from top down for $b = 0$ and $(\text{NA}, \beta) = (0.95, 1)$. The transverse and longitudinal field components and total fields are given in the columns from left to right. All intensity distributions are normalized to the maximum intensity in the focal plane for each input light mode. The size for each image is $10\lambda \times 10\lambda$.

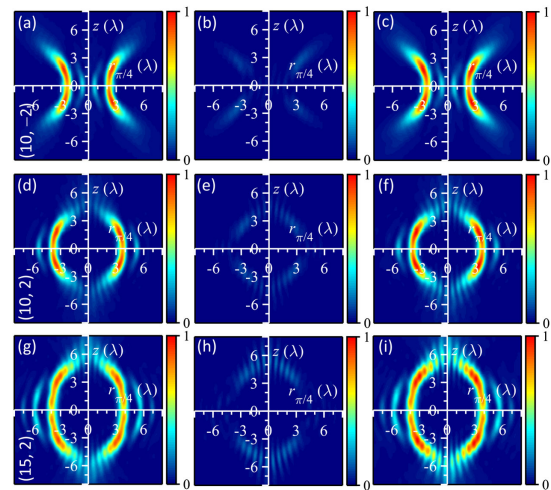


Fig. 4. Calculated electric field intensity distributions in the through-focus plane at angle $\pi/4$ to the $x - z$ plane of the tightly focused input optical fields with $(\gamma_1, \gamma_2) = (10, -2)$, $(10, 2)$, and $(15, 2)$ in the three rows from top down for $b = 0$ and $(\text{NA}, \beta) = (0.95, 1)$. The transverse and longitudinal field components and total fields are given in the columns from left to right. All intensity distributions are normalized to the maximum intensity in the through-focus plane for each input light mode. The size for each image is $16\lambda \times 16\lambda$.

To gain a deeper understanding of these highly confined fields, we calculate their energy fluxes. The three mutually perpendicular components V_{hx} , V_{hy} , and V_{hz} of the magnetic field polarization vector V_b in Eq. (3) can be similarly derived for the electric field as

$$V_{\text{hx}} = -\sqrt{\varepsilon/\mu}(\sin \phi \sin T + \cos \theta \cos \phi \cos T), \quad (9)$$

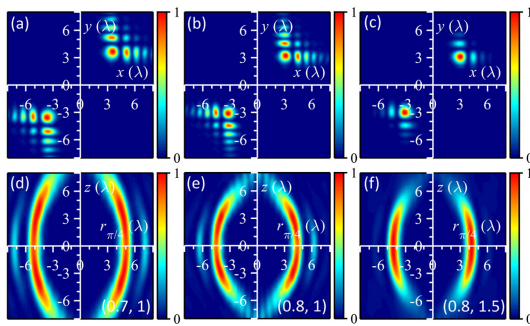


Fig. 5. Calculated electric field intensity distributions in the focal plane (top) and through-focus plane at angle $\pi/4$ to the $x-z$ plane (bottom) of the tightly focused input optical field with $(\gamma_1, \gamma_2) = (10, 2)$ when $b = 0$ under focusing conditions of $(\text{NA}, \beta) = (0.7, 1)$, $(0.8, 1)$, and $(0.8, 1.5)$ in the columns from left to right. The size for each image is $16\lambda \times 16\lambda$.

$$V_{\text{hy}} = \sqrt{\varepsilon/\mu} (\cos \phi \sin T - \cos \theta \sin \phi \cos T), \quad (10)$$

$$V_{\text{hz}} = -\sqrt{\varepsilon/\mu} \sin \theta \sin T, \quad (11)$$

where ε and μ are the electric permittivity and magnetic permeability. In terms of the 3D electric and magnetic fields expressed by Eqs. (5)–(7) and (9)–(11), the energy current is obtained from a determination of the time-averaged Poynting vector [24–26],

$$\mathbf{P} \propto \text{Re}(\mathbf{E} \times \mathbf{H}^*), \quad (12)$$

where the asterisk denotes complex conjugation. We then calculate the energy flux using Eqs. (2)–(12).

As an example, Fig. 6 shows the generalized energy fluxes of the transverse and longitudinal components in the focal and through-focus (with angle of $\pi/4$ to the $x-z$ plane) planes for the input field with $(\gamma_1, \gamma_2) = (10, 2)$ when $b = 0$. Apparently, the dual 2D Airy-shaped patterns play a dominate role for both the transverse and longitudinal components in the focal plane [Figs. 6(a) and 6(b)]. At the same time, the straight trajectories of both transverse and longitudinal energy flows are broken; they are both curved trajectories and exhibit incomplete ring patterns in the through-focus plane [Figs. 6(c) and 6(d)].

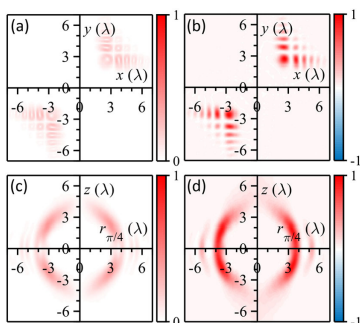


Fig. 6. Normalized energy flow distributions in the focal (top) and through-focus (bottom) planes of the tightly focused input optical fields with $(\gamma_1, \gamma_2) = (10, 2)$ when $b = 0$ and $(\text{NA}, \beta) = (0.95, 1)$. The left and right columns show, respectively, the transverse and longitudinal components.

To summarize, we proposed and demonstrated new families of highly confined structured fields assisted by specially designed PB phases. From the Richards and Wolf vectorial diffraction theory, we obtained explicit expressions for all components of the electric and magnetic field strength vectors in the focal volume of an aplanatic high NA focusing system. The calculations revealed that highly confined fields with dual 2D Airy-like patterns in the transverse plane and circular or elliptical propagation trajectories in the longitudinal plane can be achieved. Furthermore, the nano-interferometric structure of these highly confined fields is controllable and only depends on indexes γ_1 and γ_2 specifying the PB phase. Moreover, the corresponding energy flux distributions were also investigated in detail. These results not only broaden the structured highly confined fields, but also point to potential applications in areas such as nanofabrication, imaging, and optical manipulation.

Funding. National Natural Science Foundation of China (11604182); Natural Science Foundation of Shandong Province (ZR2016AB05).

REFERENCES

- M. V. Berry and N. L. Balazs, *Am. J. Phys.* **47**, 264 (1979).
- G. A. Siviloglou and D. N. Christodoulides, *Opt. Lett.* **32**, 979 (2007).
- G. A. Siviloglou, J. Broky, A. Dogariu, and D. N. Christodoulides, *Phys. Rev. Lett.* **99**, 213901 (2007).
- P. Polynkin, M. Kolesik, J. V. Moloney, G. A. Siviloglou, and D. N. Christodoulides, *Science* **324**, 229 (2009).
- T. Vettenburg, H. I. Dalgarno, J. Nytk, C. Coll-Lladó, D. E. Ferrier, T. Čižmár, F. J. Gunn-Moore, and K. Dholakia, *Nat. Methods* **11**, 541 (2014).
- S. Jia, J. C. Vaughan, and X. Zhuang, *Nat. Photonics* **8**, 302 (2014).
- J. Baumgartl, M. Mazilu, and K. Dholakia, *Nat. Photonics* **2**, 675 (2008).
- P. Zhang, Y. Hu, T. Li, D. Cannan, X. Yin, R. Morandotti, Z. Chen, and X. Zhang, *Phys. Rev. Lett.* **109**, 193901 (2012).
- M. Goutsoulas, R.-S. Penciu, and N. K. Efremidis, *Opt. Express* **26**, 18969 (2018).
- Y. Li, F. Hu, and Y. Qian, *Opt. Lett.* **44**, 1968 (2019).
- F. Maucher, S. Skupin, S. A. Gardiner, and I. G. Hughes, *Phys. Rev. Lett.* **120**, 163903 (2018).
- T. Bauer, P. Banzer, E. Karimi, S. Orlov, A. Rubano, L. Marrucci, E. Santamato, R. W. Boyd, and G. Leuchs, *Science* **347**, 964 (2015).
- Z. Man, X. Dou, and S. Fu, *Opt. Lett.* **44**, 427 (2019).
- S. Pancharatnam, *Proc. Indian Acad. Sci. A* **44**, 247 (1956).
- M. V. Berry, *J. Mod. Opt.* **34**, 1401 (1987).
- X. Xiang, J. Kim, and M. J. Escuti, *Crystals* **7**, 383 (2017).
- G. Zheng, H. Mühlenbernd, M. Kenney, G. Li, T. Zentgraf, and S. Zhang, *Nat. Nanotechnol.* **10**, 308 (2015).
- Z. Bomzon, V. Kleiner, and E. Hasman, *Opt. Lett.* **26**, 1424 (2001).
- J. P. Balthasar Mueller, N. A. Rubin, R. C. Devlin, B. Groever, and F. Capasso, *Phys. Rev. Lett.* **118**, 113901 (2017).
- Q. Zhan, *Adv. Opt. Photon.* **1**, 1 (2009).
- B. Richards and E. Wolf, *Proc. R. Soc. A* **253**, 358 (1959).
- T. Bauer, S. Orlov, U. Peschel, P. Banzer, and G. Leuchs, *Nat. Photonics* **8**, 23 (2014).
- K. Youngworth and T. Brown, *Opt. Express* **7**, 77 (2000).
- V. V. Kotlyar, A. A. Kovalev, and A. G. Nalimov, *Opt. Lett.* **43**, 2921 (2018).
- Z. Man, Z. Bai, S. Zhang, X. Li, J. Li, X. Ge, Y. Zhang, and S. Fu, *Opt. Express* **26**, 23935 (2018).
- S. S. Stafeev, V. V. Kotlyar, A. G. Nalimov, and E. S. Kozlova, *IEEE Photon. J.* **11**, 1 (2019).